ACS Photonics
pubs.acs.org/journal/apchd5 Letter

Ultra-Broadband and Omnidirectional Perfect Absorber Based on Copper Nanowire/Carbon Nanotube Hierarchical Structure

Fatemeh Kiani, Florian Sterl, Ted V. Tsoulos, Ksenia Weber, Harald Giessen, and Giulia Tagliabue*

Cite This: ACS Photonics 2020, 7, 366–374 Read Online

ACCESS | Metrics & More | Article Recommendations | Supporting Information

ABSTRACT: Zero reflection and complete light absorption are required in a wide range of applications ranging from sensing devices to solar heaters and photoelectrodes. However, simultaneously satisfying the requirements of the broadband spectrum, omnidirectionality, polarization insensitivity, and scalability is very challenging. Combining the light-trapping characteristics of microscale copper nanowires (Cu NWs) with the unique optical properties of carbon nanotubes (CNTs), we experimentally demonstrate a novel perfect absorber that has an average total reflectance of 0.75% over the broad 400−1000 nm wavelength range and an average specular reflectance as low as 0.1%. Importantly, our cactus-like, hierarchical structure retains a similar performance independently of light polarization and for a broad range of incident angles. We furthermore developed a model that elucidates how the Cu NW and CNT components synergistically contribute to the suppression of both specular and diffuse reflections while maximizing light absorption. Thanks to the scalability of the fabrication process, on the basis of the thermal oxidation and chemical vapor deposition methods, our broadband and omnidirectional perfect absorber exhibits a large potential for boosting the performance of many light-harnessing devices.

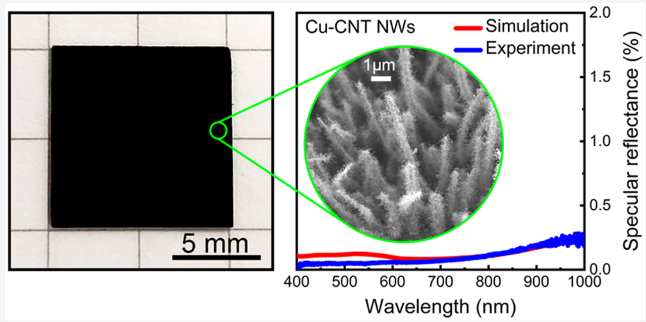

KEYWORDS: *light absorber, black coating, carbon nanotubes, perfect absorption, copper nanowires*

Perfect absorbers in the visible (vis), near-infrared (NIR), and mid-infrared (MIR) ranges are central to a variety of energy-related[1−3] and sensing-related[4,5] applications and must exhibit (1) broadband light absorption, (2) omnidirectionality, (3) polarization insensitivity, and (4) compatibility with large-scale fabrication methods.[6,7] To date, many concepts and structures have been exploited to obtain the above figures of merit of a perfect absorber.[8] A major distinction is the type of mechanism exploited for achieving absorption. On the one hand, resonant absorbers, such as plasmonic ones, exploit the strong but relatively narrowband absorption peak originating from a resonance in the structure.[9−13] To achieve a broadband spectrum, they then rely on the excitation of multiple resonances.[14,15] Thus, apart from a few exceptions,[16−20] these ultrathin absorbers require sophisticated nanopatterning procedures that significantly limit their large-scale implementation.[14] On the other hand, nonresonant nanostructured absorbers exploit the formation of a smooth effective refractive index gradient and/or enhanced multiple internal reflections within low-density arrays of long constituent elements with one or more subwavelength dimensions.[21,22] They can achieve much broader absorption spectra and can be realized with facile and scalable chemical methods.[23,24]

Carbon-based nanostructured absorbers, because of their π-band's optical transitions,[25] outperform other nonresonant absorbers such as vertically aligned Si nanostructures[23,26] in both bandwidth and absorptivity. Theoretical calculations[22] and experimental investigations suggest that an extremely low index of refraction, on the order of 1.01−1.10, as well as very low total reflectance of less than 0.045%, 1%, 0.03%, and 1% can be obtained for vertically aligned single-walled carbon nanotubes (CNTs),[22,27] multiwalled CNTs,[28,29] interlocking CNTs,[30] and graphene nanoneedle arrays,[28] respectively, across a wide spectral range from visible to MIR. However, aligned carbon nanostructures are birefringent, which makes them angle and polarization sensitive.[22,31] To remedy to the CNT birefringence and to achieve an angle- and polarization-independent optical response, a random orientation of carbon nanotubes is desirable (Figure 1a). Yet, this can compromise the low reflectivity of the coating.

One effective approach to enhance omnidirectionality and polarization insensitivity of the nanostructured absorbers, especially carbon-based ones, is to make three-dimensional hierarchical structures that combine materials of different classes, scales, and electrical/optical properties, providing a

Received: November 22, 2019
Published: January 9, 2020

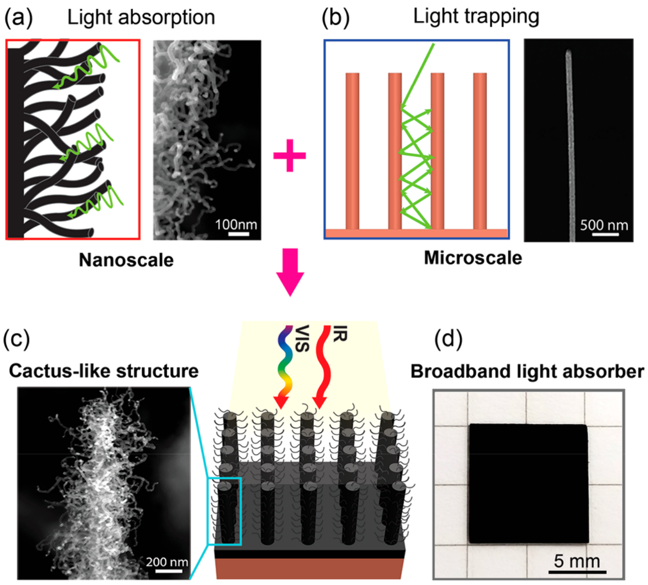

Figure 1. Schematic illustration of a hierarchical absorber concept and its experimental realization. (a) π-band mediated absorption in an effective medium of CNTs and (b) light trapping by multiple internal scattering between micrometer long Cu NWs. (c) Synergistic broadband light absorption of a forest of cactus-like Cu-CNT NWs, together with a field-emission scanning electron microscopy image of an individual cactus-like component. (d) A photographic image of the realized Cu-CNT NW structure showing its very black and rough appearance.

synergistic performance in light harvesting.[32] The superior performance of hierarchical structures is mostly attributed to their combined randomly porous and oriented micro- and nanostructure, leading to increased multiple internal reflection over a broad range of oblique incident angles and polarizations (Figure 1b).[6,21] Hierarchical carbon structures of graphdiyne nanosheets on a CuO nanowire (NW) array,[33] carbon black nanoparticles on knife-like Al_2O_3 nanoplates,[34] multiwalled CNT films on macroporous silica,[35] graphene nanosheet arrays on 3D graphene foam,[36] and multiwalled CNTs on aluminum nanostructured networks[37] were recently shown to exhibit broadband light absorption with a significantly improved incident angle independence, in some cases up to 50°.[36,37] Yet, their total reflectivity is typically higher (>2%) than vertically grown CNTs and graphene nanoneedle arrays.[33−36]

Here, we report a unique cactus-like hierarchical structure consisting of a forest of Cu NW coated with radially grown CNTs (Figure 1c) that give rise to a superblack coating material (Figure 1d). Fabricated by a facile and scalable method, which combines thermal oxidation and chemical vapor deposition techniques, our structure was shown to exhibit ultra-broadband, omnidirectional, near-to-perfect light absorption properties. Indeed, we measured an extremely low average total and specular reflectance (0.75 ± 0.26 and 0.10 ± 0.06%, respectively) over the broad 400−1000 nm range. Furthermore, we demonstrate that a similar performance is maintained up to incident angles as high as 60°, irrespective of polarization. Finally, we confirmed that total reflection remains low in the MIR range (2−10 μm). The effective medium layer-based model that we developed shows that the low reflectance indeed originates from the synergistic effect of the CNT coating on each individual Cu NW and of the Cu NW forest. Thanks to its extreme light-absorption properties, our structure could find application in a wide-range of devices for both antireflection purposes and photothermal or photocatalytic energy conversion, for example, in ultra-broadband micro-bolometer photodetectors and solar steam generation.

■ RESULTS AND DISCUSSION

The hierarchical, cactus-like Cu-CNT NW structures were obtained in three steps: (i) thermal oxidation growth of an array of vertically aligned CuO NWs on Cu substrates; (ii) hydrogen thermal reduction of CuO NWs into Cu NWs; (iii) self-catalytic chemical vapor deposition (CVD) growth of CNTs on the Cu NW array. The fabrication process is detailed in Figure 2a (see also Methods and Supporting Information S1.1). Conventionally, high-quality CNTs are grown on Cu substrates at elevated temperatures (700−900 °C) in Ar/H_2 atmospheres using extrinsic Ni catalysts[38−40] due to the poor catalytic activity of copper for CNT growth.[41] However, thermally reduced Cu NWs (Figure 2a(ii)) can easily collapse under these conditions,[42,43] and extrinsic catalysts act as impurities in the structure. To obtain our hierarchical structure, instead, we used a low-temperature self-catalytic CVD growth process by using acetylene gas (C_2H_2) as a carbon precursor due to its low decomposition temperature (~600 °C).[38] We also minimized the CNT growth time to prevent any significant morphological change of the Cu NW structure in the inert atmosphere.[42,43] Elemental analysis results of the final Cu-CNT NWs structure in Figure S1 consistently show the vast predominance of carbon and copper in the structure, indicating that the CNT-coated NWs remain in the Cu metallic state after exposure to ambient air. The very low oxygen content (ca. 2.06 wt %) can be mostly attributed to adsorbed oxygen or water molecules.[43,44]

Representative cross-sectional SEM images of the as-grown CuO NW array structure are shown in Figure 2b,c at two different magnifications. They show that thermal-oxidation growth results in a layer of highly dense and vertically aligned CuO NWs arrays with a wire length of about 30 μm on a copper oxide layer (Figure 2b), as previously reported.[45] The magnified view (Figure 2c) shows that the obtained CuO NWs have a very smooth surface with a diameter of about 100 nm. Figure 2d,e presents tilted-view SEM images of the final hierarchical Cu-CNT NW structure. Importantly, a comparison of Figure 2b,d confirms that the morphology of the NWs is largely preserved during CNT growth. A mechanical strain gradient, due to surface reduction of the NWs during the H_2 treatment process, is responsible for the slight bending of the Cu NWs.[42,43] On the contrary, samples prepared by using methane gas as the carbon precursor (growth temperature ~ 900 °C) suffered from sintering, with complete loss of the NW morphology (see Supporting Information S1.2 and Figure S3). Interestingly, the high-magnification SEM images reveal that, during our acetylene-based growth, short-length and coil-shaped CNTs[46] are radially grown on individual Cu NWs, fully covering them throughout their entire length (Figure 2e). Steric hindrance between the adjacent growing CNTs indeed results in their nonagglomerated radial alignment.[47] Some scarce carbon nanoparticles were also formed on CNTs as inevitable byproducts of the thermal CVD growth process.[48] As is evident from the close-up view SEM images (Figure S2), all the CNTs are multiwalled and have an average diameter of about 15 nm. Their growth indeed indicates that Cu NWs exhibit intrinsic high catalytic activity without the need for using an extrinsic catalyst. As Cu catalyst particles (Cu NPs)

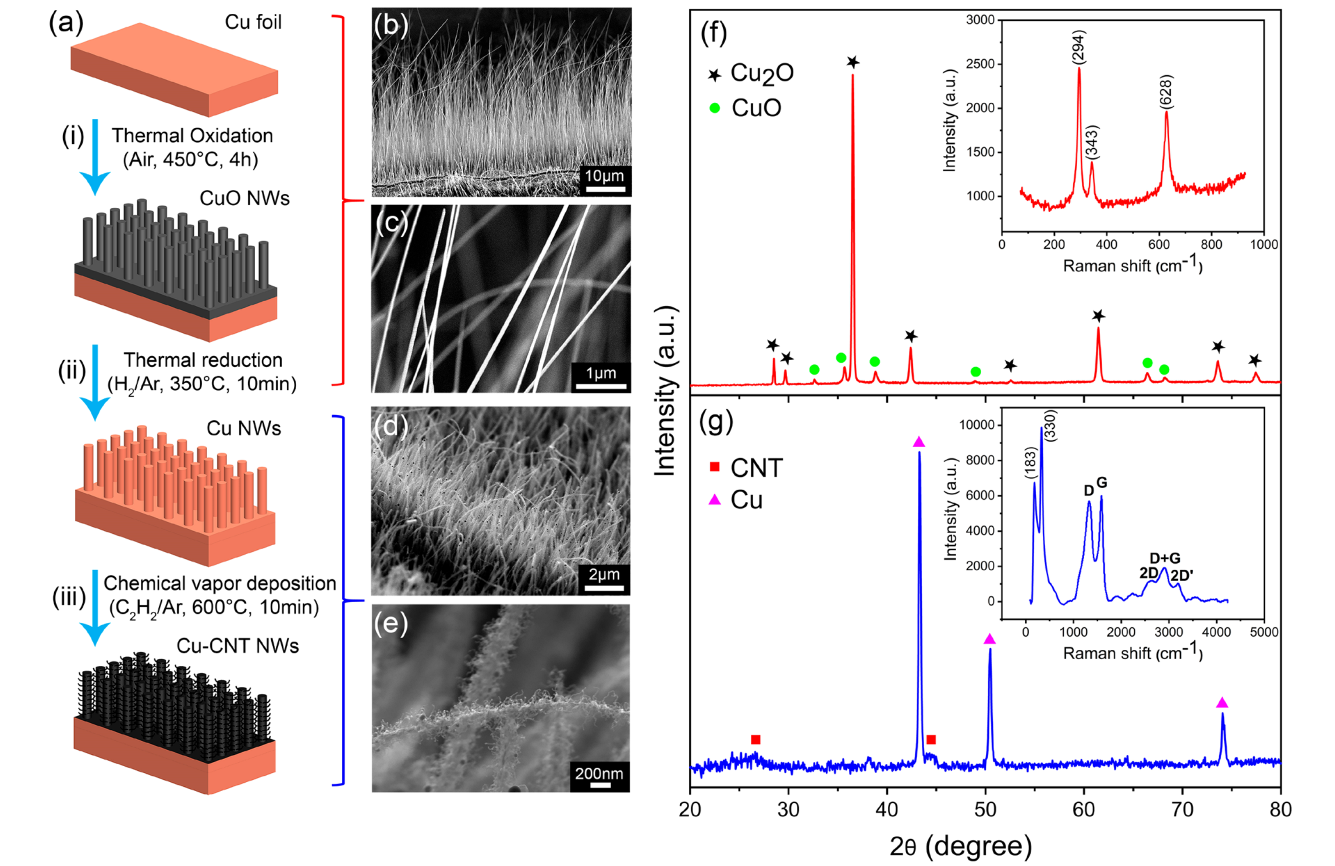

Figure 2. Fabrication process and material characterization. (a) Schematic illustration of different steps of the fabrication process. (b, c) Cross-sectional SEM images of the thermally grown CuO NW arrays on Cu substrate at low and high magnifications. (d, e) Tilted-view SEM images of the hierarchical Cu-CNT NW structure obtained by using acetylene gas at low and high magnifications. (f, g) XRD spectra of the as-grown CuO NWs and the Cu-CNT NW structures together with their corresponding Raman spectra in the inset. The Raman spectroscopy experiments were performed with a Nd:YLF laser at the excitation wavelength of 532 nm.

can be observed at the tip of the CNTs (Figure S2), we postulate a tip-growth type mechanism, contrary to a previously observed root-growth type mechanism for CNTs on a roughened Cu substrate.[49] To the best of our knowledge, only a few publications[50,51] have reported self-catalytic growth of CNTs on Cu nanostructures and none of them resulted in such a fine Cu NWs/CNTs/Cu NPs hierarchical structure. We also note here that the presence of well-dispersed and exposed nanocrystalline Cu active sites could make our high-surface area structure unique for catalytic applications.[52,53]

The composition of the structures can be more accurately determined from powder X-ray diffraction (XRD) and Raman spectroscopy (Figure 2f,g). The XRD pattern of the as-grown CuO NWs structure (Figure 2f) shows the coexistence of a mixture of monoclinic CuO and cubic Cu_2O phases, consistent with a previous observation of a parallel oxide layering structure.[45] The XRD pattern of the cactus-like Cu-CNT sample shows strong peaks at 43.3°, 50.5°, and 74.1°, corresponding to the (111), (200), and (220) reflections of face-centered-cubic Cu (JCPDS No. 04-0836), and two small broad peaks at 26.5° and 44.8° related to the (002) and (101) reflections of CNTs (JCPDS No. 08-0415). As only a weak peak of the copper oxide group is observed in the XRD graph at 38.2°, we can infer that the CuO NWs are successfully reduced into Cu NWs and that the CNT layer efficiently protects the core Cu NWs from air exposure and surface oxidation. This is in accordance with the EDS results (Figure S1) as well as previous literature reports of related systems.[37,44,54] Raman spectra further clarify the CNT structure. The inset in Figure 2g shows two dominant peaks at around 1327 and 1586 cm^{-1} related to the first-order D and G bands of CNTs, respectively.[55] Three low-intensity peaks at around 2653, 3186, and 2910 cm^{-1} can be well assigned to the overtones and combination of D and G bands, including the second-order 2D, 2D′, and D+G modes, respectively.[56−58] The D and G bands are indicative of the presence of disorder and graphitization in the CNT structure while the second-order modes indicate the long-range order present within the structure.[58] Therefore, on the basis of the sharp D peak and the broad overlapped peaks of second-order modes in the Raman spectrum, we can infer a defective multiwalled CNT structure with weak long-range order,[38] consistent with low-temperature CVD growth of CNTs[59] and formation of amorphous carbon nanoparticles in the structure.[48] Although the additional Raman features around 183 and 330 cm^{-1} (inset in Figure 2g) could not be attributed to the Cu phase, they are completely distinct from the characteristic peaks of bulk CuO, clearly visible at 294, 343, and 628 cm^{-1} (Ag, B1g, and B2g modes, respectively) in the Raman spectrum of the as-grown CuO structure[60] (inset in Figure 2f), confirming the absence of oxides in the hierarchical Cu-CNT structure.

To investigate the light-absorption characteristics of the hierarchical Cu-CNT NW array structure, wavelength-resolved reflectance spectra across the vis-to-NIR region were measured

https://dx.doi.org/10.1021/acsphotonics.9b01658
ACS Photonics 2020, 7, 366−374

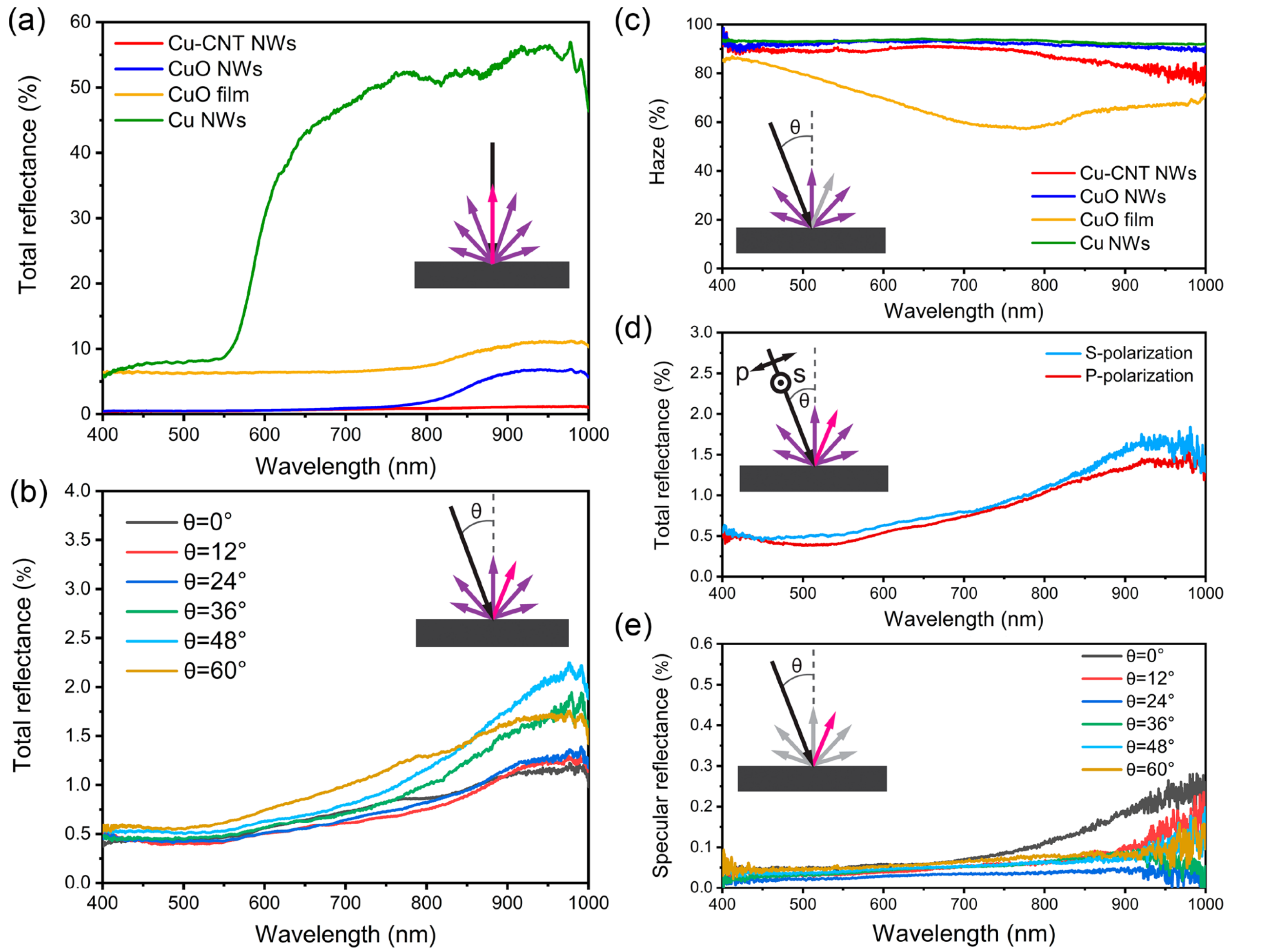

Figure 3. Experimental characterization of the optical properties of the hierarchical absorber. (a) Total reflectance spectra of the CuO NWs, CuO thin film, Cu NWs, and Cu-CNT NW structures at normal incidence. (b) Angle-resolved total reflectance spectra of the Cu-CNT NW structure at various oblique incident angles. (c) Haze ratio spectra of the CuO NWs, CuO thin film, Cu NWs, and Cu-CNT NW structures at normal incidence. (d) Total reflectance spectra of the Cu-CNT NW structure under s- and p-polarized illumination at a 50° incident angle. (e) Angle-resolved specular reflectance spectra of the Cu-CNT NW structure at various oblique incident angles. The small schematic in each graph depicts the illumination conditions (black arrow, incidence angle and polarization) and the collected reflectance component (pink arrow, specular reflection; purple arrow, diffuse reflection).

with a commercial setup (NT&C NanoMicroSpec) consisting of an inverted optical microscope, equipped with a high-NA objective (100×, 0.9 N.A.) and coupled to a grating spectrometer (see Figure S5). In all of our samples, light cannot be transmitted through the optically thick Cu substrate, and therefore, reflectance is a direct measure of absorbance, specifically absorbance = 1 − reflectance. In the following, the performance of our absorber will thus be discussed in terms of reflectance, which is the experimentally measured quantity. In these measurements, we collected both the specular and diffuse (scattered) part of the reflectance and we normalized the performance of our samples to that of a calibrated silver mirror (see the Methods and Supporting Information S2). We also compared the optical response of our cactus-like Cu-CNT NW absorber to three structures resulting from intermediate steps of our fabrication process, namely, a CuO thin film, a forest of CuO NWs, and a forest of Cu NWs (see Supporting Information S1.3 and S1.4). The total reflection spectra of the studied samples, collected for normal incidence in both the vis-to-NIR (400−1000 nm) and MIR (2−10 μm) ranges, are shown in Figures 3a and S7, respectively. The hierarchical Cu-CNT NW structure exhibits an extremely low average total reflectance of 0.75 ± 0.26% in the vis-to-NIR range and 1.37 ± 0.92% in the MIR range, clearly outperforming the other studied structures as well as previously reported hierarchical, carbon-based systems.[33−36] Comparing the featureless spectrum of the CuO film with that of the CuO NW structure, we observe that the light trapping effect of the microscale NWs[23,26] reduces the average total reflectance from a few percent to less than 1% in the 400−700 nm range. However, beyond 700 nm, the reflectance increases significantly because of the limited light absorption below the bandgap of CuO (1.4−1.7 eV).[61,62] Similarly, for the forest of Cu NWs, light-trapping by the nanowire geometry minimizes the reflection at short wavelengths, where the metal has stronger absorption due to interband transitions.[63] By comparing the response of Cu NW arrays with that of the cactus-like Cu-CNT structure, we observe that the CNT deposition dramatically suppresses the reflectance of the Cu NWs for wavelengths longer than 550 nm. Overall, these results indicate that the optical properties of our absorber are related to the synergistic combination of the NW microstructure and the CNT coating.

To fully capture the performance of our absorber, we also implemented Fourier plane-based optical measurements that

https://dx.doi.org/10.1021/acsphotonics.9b01658
ACS Photonics 2020, 7, 366−374

allow the determination of the total reflectance as a function of incident angle (from 0° up to 60°) while quantifying separately the specular and diffuse components of the signal (see Supporting Information S2, Figure S6). Impressively, for the hierarchical Cu-CNT NW structure, both the total and specular reflectance are very low and largely insensitive to the incident angle, even for values as high as 60° (total average reflectance at 60° is 1.05 ± 0.41%) (Figure 3b,e). Furthermore, our absorber is insensitive to polarization, even at a high oblique incidence angle of 50° (Figure 3d), in stark contrast to the other studied structures (Figure S8) and also to the previously studied vertically aligned CNTs.[22] We suggest that such behavior results from the suppression of the birefringence of individual CNTs due to their random orientation on each Cu NW. Considering separately the two components of the reflected light, i.e., specular and diffuse, we finally observe that, at normal incidence, the cactus-like Cu-CNT NW structures possess an extremely low and wavelength-independent average specular reflectance of 0.10 ± 0.06% across the broad 400–1000 nm specular range. Higher incident angles further improve this figure, a minimum being observed for an incident angle of 24°. This implies that the small total reflection consists primarily of diffuse light. The scattering behavior of all the structures can be analyzed on the basis of the haze ratio, defined as the ratio of diffuse reflectance to total reflectance[64] (Figures 3c and S8d–f). For normal incidence, all the studied structures behave as diffusers. The forests of Cu NWs and that of CuO NWs have the highest haze ratio (ca. 93% and 91%, respectively) across the entire spectral range. Instead, the hierarchical Cu-CNT NW structure has a very large haze across the visible range but exhibits an increase in specular reflection at wavelengths longer than ~700 nm. This optical response can be related to the relative size of the light wavelength and the structural components of the absorber, i.e., CNTs (~15 nm in diameter) and Cu NWs (~100 nm in diameter).[32] In the shorter wavelength region (400–700 nm), the Cu NWs act as individual scatterers, diffusing light in all directions. In the longer wavelength region (700–1000), instead, the size of both CNTs and Cu NWs is significantly smaller than the incident wavelength. They thus collectively behave as a homogeneous effective medium film for which the specular reflectance is increased with respect to the diffuse reflectance. We remark here, that, as is evident from Figure 3b, the average total reflectance of the hierarchical Cu-CNT NW structure remains extremely low across the entire spectrum (<1% up to 60°).

To elucidate further the origin of the exceptional light-absorption properties of our hierarchical absorber, we use an effective medium layer (EML) approach[21,65] and perform separate calculations to distinguish the contribution of the CNTs coating on each individual Cu NWs from that of the dense forest of Cu NWs.

First, using the RF module in COMSOL Multiphysics, we calculated the scattering spectrum of a standalone 30 μm-long Cu NW with and without a CNT coating under perpendicular polarization (s-polarized light) (Figure 4a). To describe the CNT coating, we binarized a high-resolution SEM image and used it to define two EMLs with different volume fractions of air and CNTs (Figure 4a; details on the numerical simulations as well as image analysis procedures and effective medium calculations can be found in Methods and Supporting Information S3.1 and S3.2). We observe that the metallic Cu NW presents resonant modes at about 610, 670, and 950 nm

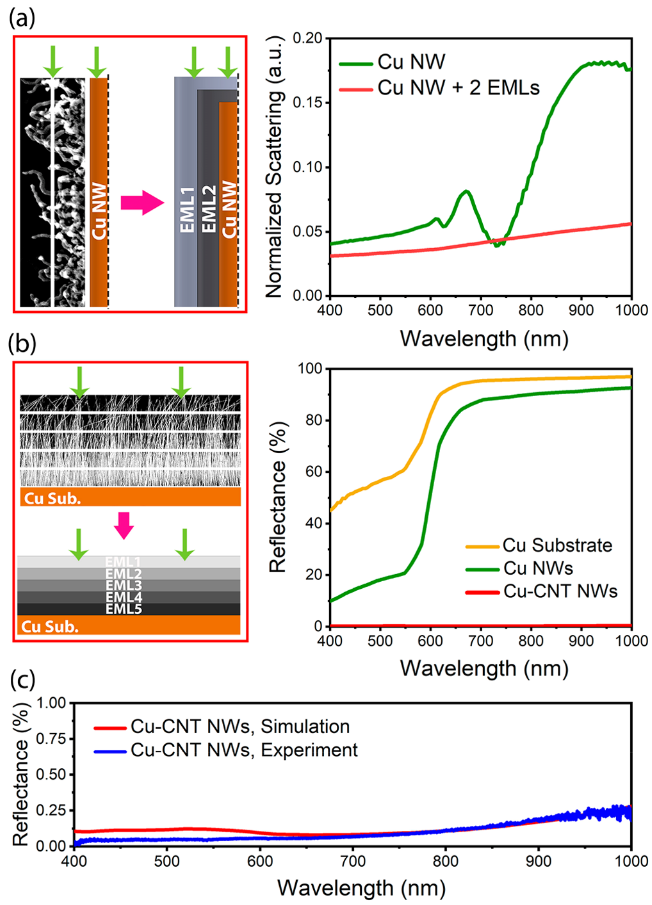

Figure 4. Modeling of the optical properties of the hierarchical absorber. (a) Schematic showing the EML determination from a binarized image of the cactus-like structure and simulated normalized scattering spectra for a 30 μm-long single Cu NW and a single Cu NW covered with two EMLs composed of different volume fractions of air and CNTs. Light is incident on the tip of the NW with polarization perpendicular to its long axis. (b) Schematic showing the transformation of a binarized SEM image into the EMLs and the simulated specular reflectance spectra for a Cu film, a forest of Cu NWs, and a forest of Cu-CNT NWs represented by five EMLs composed of different volume fractions of air and NWs. (c) A comparison between the experimental and simulated specular reflectance spectra for the Cu-CNT NW array structure.

wavelengths that significantly enhance the scattering[63] (Figures 4a and S10a), particularly in the NIR region of the spectrum (750–1000 nm). Similar resonant modes are present also for shorter Cu NWs (Figure S14), suggesting their contribution to the large diffuse reflectance of the fabricated multilength Cu NW structure (see Figure 3c). The addition of the EML coating onto the Cu NW significantly reduces its scattering, with the most pronounced effect occurring across the NIR spectral region (Figures 4a and S10b). Given that some of the Cu-CNT NWs are slightly bent (Figure 2d), we also calculated the scattering spectrum for light impinging sidewise onto single NWs with polarization parallel to their axis and observed an even larger reduction in the scattering (Figure S11). This behavior is beneficial for light absorption at very high incident angles, close to grazing incidence. Furthermore, in the latter case, we observe that the EMLs strongly increase light absorption, particularly in the NIR range (Figure S12). Indeed, for wavelengths longer than 550 nm, light reflection off the underlying Cu NWs doubles light propagation through the absorbing CNT layer.[66] Therefore, these single-NW-level simulation results show that the CNT coating plays a crucial role in both suppressing scattering and enhancing absorption.

Next, to assess the collective role of the microscale NW array onto the low reflectance of our absorber, we binarized a side-view SEM image of a NW forest and defined five EMLs with different volume fractions of air and Cu NWs or air and CNT-Cu NWs (Figure 4b and Supporting Information S3.1). Using Cu as a substrate, we then calculated the reflectance spectrum of the multilayer structure (Figure 4b). Compared to a planar Cu film, we observe that in a forest of Cu NWs the obtained graded refractive index contributes to a significant reduction in reflectance only within the spectral region of large intrinsic absorption for Cu (400−600 nm). Instead, for the hierarchical Cu-CNT NW forest, we observe a dramatic suppression of the specular reflectance (average value of $0.13 \pm 0.05\%$) across the entire vis-to-NIR spectral range (400−1000 nm), in excellent agreement with our experimental results (Figure 4c).

We conclude that the ultra-broadband and omnidirectional near-unity light-absorption properties of our hierarchical Cu-CNT NW structure originate from the synergistic contributions of the forest of nanowires and the CNT coating. On the one hand, the microscale structure of Cu NWs creates a smoothly graded refractive index that minimizes specular reflections (Figure S9c). On the other hand, the nanoscale CNT structure limits the diffuse reflectance caused by scattering of individual nanowires. These two effects combined strongly enhanced in-coupling of light into the hierarchical structure across a wide range of wavelengths and incident angles as well as for both light polarizations. Following in-coupling, light absorption is enhanced by the combination of the absorptive CNT coating with the forest of reflective Cu NWs. In fact, as discussed, Cu NWs act as back reflectors so that any unabsorbed light travels back through the CNT coating and into the NW forest, overall increasing the probability of light absorption and prolonging the optical path within the structure.

■ CONCLUSION

In summary, we experimentally demonstrated a novel hierarchical structure with ultra-broadband and omnidirectional near-unity light-absorption properties (<0.1% average specular reflection and <1% average total reflection up to a 60° incident angle within 400−1000 nm) fabricated by a facile and scalable method. Through experiments and modeling, we showed that this superior optical performance originates from the multiscale nature of the developed cactus-like structure that synergistically combines a forest of microscale Cu NWs with a nanoscale radially grown-CNT coating for each Cu NW. Indeed, the effective media created by each of these components contribute to the suppression of both specular and diffuse reflections. Furthermore, the light-trapping nature of the Cu NW forest combined with the unique optical properties of carbon-based materials maximize light absorption.

The structure could be easily scaled up to the wafer scale for industrial production, as both the thermal oxidative growth of CuO NW arrays[67,68] and the CVD growth of CNTs[27] are intrinsically scalable for large-area growth and are deployed in a continuous fashion by just changing the reactor atmosphere. The extreme light-absorption characteristics of the reported structure are promising for a wide class of devices from microbolometric photodetectors to solar-steam generators.[3,69] Also, our perfect absorber scheme can be used in optical systems for baffles and inner coatings that require suppression of strong light reflection. Furthermore, we envision that the large values of electrical and thermal conductivities of both the Cu NW and CNT components,[55,70,71] combined with the expected large local electric field enhancements[72] and the unique catalytic properties of the exposed Cu nanoparticles,[52,53] could be of great interest for novel applications in photoelectrochemical devices[73] or photoassisted field-emission devices.[74]

■ METHODS

Fabrication. A combined and continuous thermal oxidation/hydrogen thermal reduction/chemical vapor deposition technique was employed to fabricate the hierarchical Cu-CNT NW array structure (see Supporting Information S1.1). Briefly, a CuO NW array structure was first grown on a clean Cu substrate by a thermal annealing process at 450 °C for 4 h in ambient air (Figure 2a(i)). A detailed description of the growth mechanism of the CuO NWs can be found elsewhere.[75] The as-grown CuO NWs appeared black and were used as a 3D support for the later CNT branch growth, which avoids aggregation of CNTs. Before CVD growth of CNTs, a hydrogen thermal reduction process was performed on the as-grown CuO NWs at 350 °C for 10 min in a low concentration H_2 environment (300 sccm Ar/30 sccm H_2) to reduce the CuO NWs into Cu NWs, which can act as a catalyst for random growth of CNTs (Figure 2a(ii)).[42,43,76] Then, the CNTs were directly grown on the surface of Cu NW arrays via a self-catalytic mechanism at 600 °C for 10 min by using a mixture of acetylene (C_2H_2) gas (300 sccm Ar/40 sccm C_2H_2) as a carbon precursor with a low decomposition temperature (Figure 2a(iii)). After CVD growth of CNTs, the system was rapidly cooled down to room temperature (~30 K/min) under Ar cover to prevent oxidation and preserve the morphology of Cu NWs. The obtained Cu-CNT NW structure had a very black and rough appearance when inspected by the naked eye (Figure 1d).

Optical Measurements. To record reflectance spectra of structures at different incident angles, an inverted microscope (Nikon Eclipse TE2000-U) combined with a grating spectrometer via a 4-f setup was employed (see Supporting Information S2, Figure S5). A 100×, 0.9 NA objective was used to access a broad range of incident angles (up to approximately 64°). Köhler illumination was used to illuminate a small spot in the back focal plane (BFP) of the objective, corresponding to a small range of illumination angles on the sample. The angle could be controlled by moving the illuminated spot through the BFP. The 4-f setup provided access to an intermediate Fourier plane (FP), which can be used to exclude all diffuse reflectance and only record the specular component. This was done by adding an iris in the FP and aligning it to the illuminated spot in the BFP. Spectral reflectance measurements at infrared wavelengths (2−10 μm) were performed with a Bruker Vertex 80 FTIR spectrometer.

Numerical Simulation. Effective medium theory approximation and the RF module of the COMSOL Multiphysics V5.3 software package were used to simulate the scattering and the reflectivity of Cu-CNT NWs at both the single nanowire and the array scale level as a function of wavelength (see Supporting Information S3). To simulate the effect of the CNT layer on the scattering of a single Cu NW, a 2D numerical electromagnetic model was developed and the scattering behavior was modeled for a 30 μm-long cylindrical Cu NW wrapped with two EMLs of CNTs (see Supporting Information S3.2.1 and Figure S9a). We used a scattering boundary condition to terminate the simulated domain and avoid any reflection from the boundaries. The system was studied for light propagation both perpendicular and parallel to the wire long axis with polarization parallel and perpendicular to it, respectively. To simulate the effect of a forest of Cu NWs with and without a CNT coating and calculate its reflectance, a 2D unit cell model was employed. A Floquet boundary condition was used to simulate an infinite film consisting of a Cu back reflector and five EMLs with an overall height of 30 μm (see Supporting Information S3.2.2 and Figure S9b). A port boundary condition was used for excitation and reflection calculations. The percentage of reflected light was obtained by calculating the outgoing power from port 1 at the top of the unit cell. The wavelength-dependent complex refractive indices for CNT (considered as graphite) and Cu were taken from refs 77 and 78.

■ ASSOCIATED CONTENT

Supporting Information

The Supporting Information is available free of charge at https://pubs.acs.org/doi/10.1021/acsphotonics.9b01658.

Additional information about the growth methodology for the structures together with their corresponding SEM images and the EDS mapping results; the employed reflectance measurement technique with the reflectance measurement results for the structures across the vis-to-NIR range and the MIR of the spectrum; effective medium approximation and the image analysis results; numerical modeling of the optical properties of the structures together with the simulation results (PDF)

■ AUTHOR INFORMATION

Corresponding Author

Giulia Tagliabue – *École Polytechnique Fédérale de Lausanne, Lausanne, Switzerland;* orcid.org/0000-0003-4587-728X; Email: giulia.tagliabue@epfl.ch

Other Authors

Fatemeh Kiani – *École Polytechnique Fédérale de Lausanne, Lausanne, Switzerland*

Florian Sterl – *University of Stuttgart, Stuttgart, Germany;* orcid.org/0000-0002-1025-6777

Ted V. Tsoulos – *École Polytechnique Fédérale de Lausanne, Lausanne, Switzerland;* orcid.org/0000-0003-2531-9723

Ksenia Weber – *University of Stuttgart, Stuttgart, Germany;* orcid.org/0000-0002-9836-8457

Harald Giessen – *University of Stuttgart, Stuttgart, Germany*

Complete contact information is available at: https://pubs.acs.org/10.1021/acsphotonics.9b01658

Notes

The authors declare no competing financial interest.

■ ACKNOWLEDGMENTS

We would like to express our appreciation to Arnaud Magrez and the crystal growth facility at EPFL for giving us access to the CVD tube furnace as well as XRD and Raman spectroscopy facilities. We are also very grateful to the Interdisciplinary Center for Electron Microscopy (CIME) at EPFL for providing us with electron microscopy facilities. We furthermore gratefully acknowledge financial support by the Deutsche Forschungsgemeinschaft (SPP1839 - Tailored Disorder) as well as ERC ADG Complex Plus BMBF (Printoptics). We also extend our special thanks to Milad Sabzehparvar for his advice during the initial steps of this research work.

■ REFERENCES

(1) Zhou, L.; Tan, Y.; Ji, D.; Zhu, B.; Zhang, P.; Xu, J.; Gan, Q.; Yu, Z.; Zhu, J. Self-assembly of highly efficient, broadband plasmonic absorbers for solar steam generation. *Sci. Adv.* **2016**, *2* (4), No. e1501227.

(2) Zhou, L.; Tan, Y.; Zhu, J. Broadband Plasmonic Absorbers for Highly Efficient Solar Steam Generation. In *Optical Nanostructures and Advanced Materials for Photovoltaics*; Optical Society of America: 2015; p PW3B. 3.

(3) Dongare, P. D.; Alabastri, A.; Neumann, O.; Nordlander, P.; Halas, N. J. Solar thermal desalination as a nonlinear optical process. *Proc. Natl. Acad. Sci. U. S. A.* **2019**, *116*, 13182.

(4) Liu, Y.; Wang, F.; Wang, X.; Wang, X.; Flahaut, E.; Liu, X.; Li, Y.; Wang, X.; Xu, Y.; Shi, Y.; et al. Planar carbon nanotube–graphene hybrid films for high-performance broadband photodetectors. *Nat. Commun.* **2015**, *6*, 8589.

(5) Liu, Y.; Yin, J.; Wang, P.; Hu, Q.; Wang, Y.; Xie, Y.; Zhao, Z.; Dong, Z.; Zhu, J.-L.; Chu, W.; et al. High-performance, ultra-broadband, ultraviolet to terahertz photodetectors based on suspended carbon nanotube films. *ACS Appl. Mater. Interfaces* **2018**, *10* (42), 36304–36311.

(6) Ghobadi, A.; Hajian, H.; Dereshgi, S. A.; Bozok, B.; Butun, B.; Ozbay, E. Disordered nanohole patterns in metal-insulator multilayer for ultra-broadband light absorption: atomic layer deposition for lithography free highly repeatable large scale multilayer growth. *Sci. Rep.* **2017**, *7* (1), 15079.

(7) Dong, X.; Chen, L. Ultrabroadband Plasmonic Absorber Based on Biomimetic Compound Eye Structures. *IEEE Photonics J.* **2018**, *10* (1), 1–7.

(8) Khodasevych, I. E.; Wang, L.; Mitchell, A.; Rosengarten, G. Micro-and nanostructured surfaces for selective solar absorption. *Adv. Opt. Mater.* **2015**, *3* (7), 852–881.

(9) Tittl, A.; Harats, M. G.; Walter, R.; Yin, X.; Schäferling, M.; Liu, N.; Rapaport, R.; Giessen, H. Quantitative angle-resolved small-spot reflectance measurements on plasmonic perfect absorbers: impedance matching and disorder effects. *ACS Nano* **2014**, *8* (10), 10885–10892.

(10) Walter, R.; Tittl, A.; Berrier, A.; Sterl, F.; Weiss, T.; Giessen, H. Large-Area Low-Cost Tunable Plasmonic Perfect Absorber in the Near Infrared by Colloidal Etching Lithography. *Adv. Opt. Mater.* **2015**, *3* (3), 398–403.

(11) Akselrod, G. M.; Huang, J.; Hoang, T. B.; Bowen, P. T.; Su, L.; Smith, D. R.; Mikkelsen, M. H. Large-area metasurface perfect absorbers from visible to near-infrared. *Adv. Mater.* **2015**, *27* (48), 8028–8034.

(12) Li, W.; Valentine, J. Metamaterial perfect absorber based hot electron photodetection. *Nano Lett.* **2014**, *14* (6), 3510–3514.

(13) Liu, N.; Mesch, M.; Weiss, T.; Hentschel, M.; Giessen, H. Infrared perfect absorber and its application as plasmonic sensor. *Nano Lett.* **2010**, *10* (7), 2342–2348.

(14) Yang, C.; Ji, C.; Shen, W.; Lee, K.-T.; Zhang, Y.; Liu, X.; Guo, L. J. Compact multilayer film structures for ultrabroadband,

omnidirectional, and efficient absorption. *ACS Photonics* **2016**, 3 (4), 590−596.

(15) Aydin, K.; Ferry, V. E.; Briggs, R. M.; Atwater, H. A. Broadband polarization-independent resonant light absorption using ultrathin plasmonic super absorbers. *Nat. Commun.* **2011**, *2*, 517.

(16) Zhang, H.; Guan, C.; Luo, J.; Yuan, Y.; Song, N.; Zhang, Y.; Fang, J.; Liu, H. A Facile Film-Nanoctahedron Assembly Route to Plasmonic Metamaterial Absorbers at Visible Frequencies. *ACS Appl. Mater. Interfaces* **2019**, *11*, 20241.

(17) Ng, C.; Yap, L. W.; Roberts, A.; Cheng, W.; Gómez, D. E. Black gold: broadband, high absorption of visible light for photochemical systems. *Adv. Funct. Mater.* **2017**, *27* (2), 1604080.

(18) Tagliabue, G.; Eghlidi, H.; Poulikakos, D. Facile multifunctional plasmonic sunlight harvesting with tapered triangle nanopatterning of thin films. *Nanoscale* **2013**, *5* (20), 9957−9962.

(19) Tagliabue, G.; Eghlidi, H.; Poulikakos, D. Rapid-response low infrared emission broadband ultrathin plasmonic light absorber. *Sci. Rep.* **2015**, *4*, 7181.

(20) Ghobadi, A.; Dereshgi, S. A.; Hajian, H.; Birant, G.; Butun, B.; Bek, A.; Ozbay, E. 97% light absorption in an ultrabroadband frequency range utilizing an ultrathin metal layer: randomly oriented, densely packed dielectric nanowires as an excellent light trapping scaffold. *Nanoscale* **2017**, *9* (43), 16652−16660.

(21) Karadan, P.; Anappara, A. A.; Moorthy, V.; Narayana, C.; Barshilia, H. C. Improved broadband and omnidirectional light absorption in silicon nanopillars achieved through gradient mesoporosity induced leaky waveguide modulation. *RSC Adv.* **2016**, *6* (110), 109157−109167.

(22) Yang, Z.-P.; Ci, L.; Bur, J. A.; Lin, S.-Y.; Ajayan, P. M. Experimental observation of an extremely dark material made by a low-density nanotube array. *Nano Lett.* **2008**, *8* (2), 446−451.

(23) Huang, Y.-F.; Chattopadhyay, S.; Jen, Y.-J.; Peng, C.-Y.; Liu, T.-A.; Hsu, Y.-K.; Pan, C.-L.; Lo, H.-C.; Hsu, C.-H.; Chang, Y.-H.; et al. Improved broadband and quasi-omnidirectional anti-reflection properties with biomimetic silicon nanostructures. *Nat. Nanotechnol.* **2007**, *2* (12), 770.

(24) Anguita, J. V.; Ahmad, M.; Haq, S.; Allam, J.; Silva, S. R. P. Ultra-broadband light trapping using nanotextured decoupled graphene multilayers. *Sci. Adv.* **2016**, *2* (2), No. e1501238.

(25) Taft, E.; Philipp, H. Optical properties of graphite. *Phys. Rev.* **1965**, *138* (1A), A197.

(26) Steglich, M.; Käsebier, T.; Höger, I.; Füchsel, K.; Tünnermann, A.; Kley, E.-B. Black silicon nanostructures on silicon thin films prepared by reactive ion etching. *Chin. Opt. Lett.* **2013**, *11*, S10502.

(27) Mizuno, K.; Ishii, J.; Kishida, H.; Hayamizu, Y.; Yasuda, S.; Futaba, D. N.; Yumura, M.; Hata, K. A black body absorber from vertically aligned single-walled carbon nanotubes. *Proc. Natl. Acad. Sci. U. S. A.* **2009**, *106* (15), 6044−6047.

(28) Matsumoto, T.; Koizumi, T.; Kawakami, Y.; Okamoto, K.; Tomita, M. Perfect blackbody radiation from a graphene nanostructure with application to high-temperature spectral emissivity measurements. *Opt. Express* **2013**, *21* (25), 30964−30974.

(29) Wang, X.; Flicker, J.; Lee, B. J.; Ready, W.; Zhang, Z. Visible and near-infrared radiative properties of vertically aligned multi-walled carbon nanotubes. *Nanotechnology* **2009**, *20* (21), 215704.

(30) Yang, Z.-P.; Hsieh, M.-L.; Bur, J. A.; Ci, L.; Hanssen, L. M.; Wilthan, B.; Ajayan, P. M.; Lin, S.-Y. Experimental observation of extremely weak optical scattering from an interlocking carbon nanotube array. *Appl. Opt.* **2011**, *50* (13), 1850−1855.

(31) Garcia-Vidal, F.; Pitarke, J.; Pendry, J. Effective medium theory of the optical properties of aligned carbon nanotubes. *Phys. Rev. Lett.* **1997**, *78* (22), 4289.

(32) Ho, C.-H.; Lien, D.-H.; Chang, H.-C.; Lin, C.-A.; Kang, C.-F.; Hsing, M.-K.; Lai, K.-Y.; He, J.-H. Hierarchical structures consisting of SiO_2 nanorods and p-GaN microdomes for efficiently harvesting solar energy for InGaN quantum well photovoltaic cells. *Nanoscale* **2012**, *4* (23), 7346−7349.

(33) Gao, X.; Ren, H.; Zhou, J.; Du, R.; Yin, C.; Liu, R.; Peng, H.; Tong, L.; Liu, Z.; Zhang, J. Synthesis of hierarchical graphdiyne-based architecture for efficient solar steam generation. *Chem. Mater.* **2017**, *29* (14), 5777−5781.

(34) Xu, N.; Li, J.; Wang, Y.; Fang, C.; Li, X.; Wang, Y.; Zhou, L.; Zhu, B.; Wu, Z.; Zhu, S.; et al. A water lily−inspired hierarchical design for stable and efficient solar evaporation of high-salinity brine. *Sci. Adv.* **2019**, *5* (7), No. eaaw7013.

(35) Wang, Y.; Zhang, L.; Wang, P. Self-floating carbon nanotube membrane on macroporous silica substrate for highly efficient solar-driven interfacial water evaporation. *ACS Sustainable Chem. Eng.* **2016**, *4* (3), 1223−1230.

(36) Ren, H.; Tang, M.; Guan, B.; Wang, K.; Yang, J.; Wang, F.; Wang, M.; Shan, J.; Chen, Z.; Wei, D.; et al. Hierarchical graphene foam for efficient omnidirectional solar−thermal energy conversion. *Adv. Mater.* **2017**, *29* (38), 1702590.

(37) Cui, K.; Wardle, B. L. Breakdown of Native Oxide Enables Multifunctional, Free-Form Carbon Nanotube−Metal Hierarchical Architectures. *ACS Appl. Mater. Interfaces* **2019**, *11* (38), 35212−35220.

(38) Atthipalli, G. *Growth of Aligned Carbon Nanotubes on Copper Substrates*. Ph.D. Thesis, University of Pittsburgh, 2011.

(39) Yin, X.; Wang, Q.; Lou, C.; Zhang, X.; Lei, W. Growth of multi-walled CNTs emitters on an oxygen-free copper substrate by chemical-vapor deposition. *Appl. Surf. Sci.* **2008**, *254* (20), 6633−6636.

(40) Jain, V.; Tripathi, A. K.; Saini, K.; Deva, D.; Lahiri, I. Copper nanowire−carbon nanotube hierarchical structure for enhanced field emission. *J. Mater. Sci.: Mater. Electron.* **2018**, *29* (16), 13620−13630.

(41) Deck, C. P.; Vecchio, K. Prediction of carbon nanotube growth success by the analysis of carbon−catalyst binary phase diagrams. *Carbon* **2006**, *44* (2), 267−275.

(42) Du, L.; Shi, T.; Su, L.; Tang, Z.; Liao, G. Hydrogen thermal reductive Cu nanowires in low temperature Cu−Cu bonding. *J. Micromech. Microeng.* **2017**, *27* (7), 075019.

(43) Han, J.-W.; Lohn, A.; Kobayashi, N. P.; Meyyappan, M. Evolutional transformation of copper oxide nanowires to copper nanowires by a reduction technique. *Mater. Express* **2011**, *1* (2), 176−180.

(44) Arzi, M.; Sabzehparvar, M.; Sadrnezhaad, S. K.; Amin, M. H. Nanostructural study of NiTi−TiO_2−C core−shell nanoparticles generated by spark discharge method. *Appl. Phys. A: Mater. Sci. Process.* **2018**, *124* (9), 625.

(45) Kiani, F.; Astani, N. A.; Rahighi, R.; Tayyebi, A.; Tayebi, M.; Khezri, J.; Hashemi, E.; Rothlisberger, U.; Simchi, A. Effect of graphene oxide nanosheets on visible light-assisted antibacterial activity of vertically-aligned copper oxide nanowire arrays. *J. Colloid Interface Sci.* **2018**, *521*, 119−131.

(46) Thirumal, V.; Pandurangan, A.; Jayavel, R.; Krishnamoorthi, S.; Ilangovan, R. Synthesis of nitrogen doped coiled double walled carbon nanotubes by chemical vapor deposition method for supercapacitor applications. *Curr. Appl. Phys.* **2016**, *16* (8), 816−825.

(47) Bower, C.; Zhu, W.; Jin, S.; Zhou, O. Plasma-induced alignment of carbon nanotubes. *Appl. Phys. Lett.* **2000**, *77* (6), 830−832.

(48) Schünemann, C.; Schäffel, F.; Bachmatiuk, A.; Queitsch, U.; Sparing, M.; Rellinghaus, B.; Lafdi, K.; Schultz, L.; Büchner, B.; Rümmeli, M. H. Catalyst poisoning by amorphous carbon during carbon nanotube growth: Fact or fiction? *ACS Nano* **2011**, *5* (11), 8928−8934.

(49) Jang, L.-W.; Shim, J.; Son, D. I.; Cho, H.; Zhang, L.; Zhang, J.; Menghini, M.; Locquet, J.-P.; Seo, J. W. Simultaneous growth of three-dimensional carbon nanotubes and ultrathin graphite networks on copper. *Sci. Rep.* **2019**, *9* (1), 1−9.

(50) Takagi, D.; Homma, Y.; Hibino, H.; Suzuki, S.; Kobayashi, Y. Single-walled carbon nanotube growth from highly activated metal nanoparticles. *Nano Lett.* **2006**, *6* (12), 2642−2645.

(51) Zhou, W.; Han, Z.; Wang, J.; Zhang, Y.; Jin, Z.; Sun, X.; Zhang, Y.; Yan, C.; Li, Y. Copper catalyzing growth of single-walled carbon nanotubes on substrates. *Nano Lett.* **2006**, *6* (12), 2987−2990.

https://dx.doi.org/10.1021/acsphotonics.9b01658
ACS Photonics 2020, 7, 366−374

(52) Luc, W.; Fu, X.; Shi, J.; Lv, J.-J.; Jouny, M.; Ko, B. H.; Xu, Y.; Tu, Q.; Hu, X.; Wu, J. Two-dimensional copper nanosheets for electrochemical reduction of carbon monoxide to acetate. *Nat. Catal.* **2019**, *2* (5), 423.
(53) Zhang, X.; Fu, A.; Chen, X.; Liu, L.; Ren, L.; Tong, L.; Ye, J. Highly efficient Cu induced photocatalysis for visible-light hydrogen evolution. *Catal. Today* **2019**, *335*, 166−172.
(54) Ahn, Y.; Jeong, Y.; Lee, D.; Lee, Y. Copper nanowire−graphene core−shell nanostructure for highly stable transparent conducting electrodes. *ACS Nano* **2015**, *9* (3), 3125−3133.
(55) Reich, S.; Thomsen, C.; Maultzsch, J. *Carbon nanotubes: basic concepts and physical properties*; John Wiley & Sons: 2008.
(56) Thomsen, C. Second-order Raman spectra of single and multiwalled carbon nanotubes. *Phys. Rev. B: Condens. Matter Mater. Phys.* **2000**, *61* (7), 4542.
(57) Travessa, D. N.; Silva, F. S. d.; Cristovan, F. H.; Jorge, A. M., Jr; Cardoso, K. R. Ag ion decoration for surface modifications of multiwalled carbon nanotubes. *Mater. Res.* **2014**, *17* (3), 687−693.
(58) Bîru, E. I.; Iovu, H. Graphene Nanocomposites Studied by Raman Spectroscopy. *Raman Spectroscopy* **2018**, 179.
(59) Lim, Y. D.; Avramchuck, A. V.; Grapov, D.; Tan, C. W.; Tay, B. K.; Aditya, S.; Labunov, V. Enhanced carbon nanotubes growth using nickel/ferrocene-hybridized catalyst. *ACS Omega* **2017**, *2* (9), 6063−6071.
(60) Huang, J.; Li, H.; Zhu, Y.; Cheng, Q.; Yang, X.; Li, C. Sculpturing metal foams toward bifunctional 3D copper oxide nanowire arrays for pseudo-capacitance and enzyme-free hydrogen peroxide detection. *J. Mater. Chem. A* **2015**, *3* (16), 8734−8741.
(61) Hansen, B. J.; Kouklin, N.; Lu, G.; Lin, I.-K.; Chen, J.; Zhang, X. Transport, analyte detection, and opto-electronic response of p-type CuO nanowires. *J. Phys. Chem. C* **2010**, *114* (6), 2440−2447.
(62) Jeyarani, W. J.; Tenkyong, T.; Bachan, N.; Kumar, D. A.; Shyla, J. M. An investigation on the tuning effect of glucose-capping on the size and bandgap of CuO nanoparticles. *Adv. Powder Technol.* **2016**, *27* (2), 338−346.
(63) Wang, H.; Tam, F.; Grady, N. K.; Halas, N. J. Cu nanoshells: effects of interband transitions on the nanoparticle plasmon resonance. *J. Phys. Chem. B* **2005**, *109* (39), 18218−18222.
(64) Wang, H.-P.; Periyanagounder, D.; Li, A.-C.; He, J.-H. Fabrication of silicon hierarchical structures for solar cell applications. *IEEE Access* **2019**, *7*, 19395−19400.
(65) Jayaprakash, R.; Ajagunna, D.; Germanis, S.; Androulidaki, M.; Tsagaraki, K.; Georgakilas, A.; Pelekanos, N. Extraction of absorption coefficients from as-grown GaN nanowires on opaque substrates using all-optical method. *Opt. Express* **2014**, *22* (16), 19555−19566.
(66) Peng, H.; Luo, Y.; Ying, X.; Pu, Y.; Jiang, Y.; Xu, J.; Liu, Z. Broadband and highly absorbing multilayer structure in mid-infrared. *Appl. Opt.* **2016**, *55* (31), 8833−8838.
(67) Zhu, Y.; Yu, T.; Cheong, F.; Xu, X.; Lim, C.; Tan, V.; Thong, J.; Sow, C. Large-scale synthesis and field emission properties of vertically oriented CuO nanowire films. *Nanotechnology* **2005**, *16* (1), 88.
(68) Mumm, F.; Sikorski, P. Oxidative fabrication of patterned, large, non-flaking CuO nanowire arrays. *Nanotechnology* **2011**, *22* (10), 105605.
(69) Neumann, O.; Neumann, A. D.; Tian, S.; Thibodeaux, C.; Shubhankar, S.; Müller, J.; Silva, E.; Alabastri, A.; Bishnoi, S. W.; Nordlander, P.; et al. Combining solar steam processing and solar distillation for fully off-grid production of cellulosic bioethanol. *ACS Energy Letters* **2017**, *2* (1), 8−13.
(70) Ding, S.; Tian, Y.; Jiu, J.; Suganuma, K. Highly conductive and transparent copper nanowire electrodes on surface coated flexible and heat-sensitive substrates. *RSC Adv.* **2018**, *8* (4), 2109−2115.
(71) Bhanushali, S.; Jason, N. N.; Ghosh, P.; Ganesh, A.; Simon, G. P.; Cheng, W. Enhanced thermal conductivity of copper nanofluids: the effect of filler geometry. *ACS Appl. Mater. Interfaces* **2017**, *9* (22), 18925−18935.
(72) Hu, H.; Zhang, D.; Liu, Y.; Yu, W.; Guo, T. Highly enhanced field emission from CuO nanowire arrays by coating of carbon nanotube network films. *Vacuum* **2015**, *115*, 70−74.
(73) DuChene, J. S.; Tagliabue, G.; Welch, A. J.; Cheng, W.-H.; Atwater, H. A. Hot hole collection and photoelectrochemical CO2 reduction with plasmonic Au/p-GaN photocathodes. *Nano Lett.* **2018**, *18* (4), 2545−2550.
(74) Wang, P.; Krasavin, A. V.; Nasir, M. E.; Dickson, W.; Zayats, A. V. Reactive tunnel junctions in electrically driven plasmonic nanorod metamaterials. *Nat. Nanotechnol.* **2018**, *13* (2), 159.
(75) Xiang, L.; Guo, J.; Wu, C.; Cai, M.; Zhou, X.; Zhang, N. A brief review on the growth mechanism of CuO nanowires via thermal oxidation. *J. Mater. Res.* **2018**, *33* (16), 2264−2280.
(76) Rashid, N. M.; Kishi, N.; Soga, T. Effects of reduction temperature on copper nanowires growth by thermal reduction of copper oxide nanowires. *Mod. Phys. Lett. B* **2016**, *30* (17), 1650193.
(77) Djurišić, A. B.; Li, E. H. Optical properties of graphite. *J. Appl. Phys.* **1999**, *85* (10), 7404−7410.
(78) Johnson, P. B.; Christy, R.-W. Optical constants of the noble metals. *Phys. Rev. B* **1972**, *6* (12), 4370.